2024 IEEE International Conference on Robotics and Automation (ICRA 2024)
May 13-17, 2024. Yokohama, Japan

A Magnetic Continuum Robot with In-situ Magnetic Reprogramming Capability

Junnan Xue[1,†], Moqiu Zhang[1,†], Xurui Liu[1], Jiaqi Zhu[1], Yanfei Cao[1] and Li Zhang[1,2,3,4], *Fellow, IEEE*

***Abstract*— Magnetic continuum robots (MCR) have shown great potential in minimally invasive interventions because they can be actively and remotely navigated through complex in vivo environments. However, the deformation capability of current MCRs is limited by fixed magnetization configurations, preventing them from accessing hard-to-reach areas. This is due to the fact that under a global magnetic field, fixed magnetization configuration causes the magnets on the MCRs exposed to coupled magnetic forces and torques, resulting in a lack of controllable degrees of freedom. Here, we introduce a reprogrammable magnetic continuum robot (RMCR) enabled by magnetic reprogramming modules (MRM). Actuated by shape memory alloys, the magnetic moment direction of MRMs can be selectively reprogrammed in real-time and in-situ. Magnetic reprogramming capabilities enable the RMCR to achieve complex shape transformations. Results show that the range of motion in the tip direction of the RMCR increases by 193% compared with regular MCR. Besides, MRMs on the RMCR can achieve active attraction and separation under simple magnetic fields. The reprogramming process of the RMCR is theoretically investigated. A design methodology for MRMs is then proposed and the fabrication process of RMCR is described in detail. Furthermore, a kinematic model of the RMCR is established, simulated, and experimentally validated.**

I. Introduction

Magnetic continuum robot (MCR) has attracted sustained interest because it combines the advantages of safety and compliance of soft robots with remote and contact-less feature of magnetic actuation technology [1]–[3]. Compared with tendon driven, hydraulic, and pneumatic robots, which require complex robot structure and transmission mechanisms, MCR utilize non-contact actuating forces generated from magnets inside the robots exerted by magnetic fields, thus enabling robot miniaturization [3]–[5].

Many efforts have been made to improve the dexterity and functionality of MCRs. One way is to increase the degrees of freedom (DoF) of the magnetic actuation systems. Electromagnetic coils based actuation system can generate flexible magnetic field with switching function [6], and has been used in various areas of magnetically controlled robotics [7]–[10]. Instead of using position-fixed coils, movable coil system can further expand the working space [11]–[13]. Compared with electromagnetic systems, permanent magnet systems can generate stronger magnetic field, which means the actuated robots can be further reduced in size or navigated over a greater distance for better integration with existing medical imaging systems [14]–[18].

Although magnetic actuation systems can produce flexible magnetic fields, the maximum actuated DoF in homogeneous quasi-static magnetic field is reported to be eight [19]. Therefore, another way to further increase the flexibility of an MCR is to optimize its structure design. Many different structures of MCR have been proposed, from a single magnet, to multiple magnets, opposite magnets, continuously magnetized and customized-magnetized configurations. Different magnetization configurations can grant the MCRs with different deformation capabilities. Compared with a single magnet [20], [21], multiple magnets have more controllable DoF [22]–[24]. By programming a heterogeneous magnetic field, the multi-segment deformation of the MCR can be precisely controlled. The opposite magnetization configuration grants MCR with special deformations, such as J, C, and S shapes [25], [26]. MRC with continuous magnetization has less stiffness and can pass through areas of smaller radius of curvature [3], [27]. Combined with patient-specific preoperative scan, the magnetization profiles of MCR can also be customized [28]. The customized MCR can achieve specific deformations, thereby reducing the unnecessary contact with surrounding anatomical structures. Different modeling and control methods have also been proposed for different MCR and demonstrated high accuracy [8], [20], [29], [30].

Instead of pre-programming the magnetization configurations of robots [31]–[33], the magnetic reprogramming technology allows the magnetization pattern of the robot to be altered in-situ. Many approaches have been proposed to reprogram the magnetization of the robots, such as heating the magnetic agent above its Curie temperature [34], melting the temperature-responsive material wrapped around the magnetic agent [35]. When excited to a reprogrammable state, the magnetization direction of the robots can be reprogrammed by applying an external magnetic field. The magnetization of single domain nanomagnets with different coercivities can also be reprogrammed by applying a specific sequence of magnetic fields [36]. By using the magnetic reprogramming

This work was supported in part by the Croucher Foundation Grant with Ref. No. CAS20403, in part by the Research Impact Fund (project no.R4015-21) and Research Fellow Scheme (project no. RFS2122-4S03) from the Research Grants Council (RGC) of Hong Kong, in part by the RGC Collaborative Research Fund with Project No. C1134-20GF, in part by the CUHK internal grants. The authors also thank support from the SIAT-CUHK Joint Laboratory of Robotics and Intelligent Systems, and the Multiscale Medical Robotics Center (MRC), InnoHK, at the Hong Kong Science Park. (†These authors contributed equally to this work) (*Corresponding author: Li Zhang)

[1]Department of Mechanical and Automation Engineering, The Chinese University of Hong Kong (CUHK), Shatin NT, Hong Kong, China. lizhang@mae.cuhk.edu.hk

[2]Chow Yuk Ho Technology Center for Innovative Medicine, The Chinese University of Hong Kong, Hong Kong, China.

[3]CUHK T Stone Robotics Institute, The Chinese University of Hong Kong, Hong Kong, China.

[4]Department of Surgery, The Chinese University of Hong Kong, Hong Kong, China.

technology, magnetic robots can achieve different types of deformations under a simple magnetic field without the need for remanufacturing.

In this work, we introduce a reprogrammable magnetic continuum robot (RMCR) with multi-modal deformation capability and enhanced workspace. The RMCR is composed of several magnetic reprogrammable modules (MRM) and a flexible body. By controlling the magnetization of the MRM in-situ, the RMCR can achieve complex deformations as shown in Fig.1. Furthermore, MRMs can be actively controlled to attract and lock with each other. The assembled configuration can be controlled stably under magnetic field without separation. By reprogramming the magnetization of MRMs again, the assembled MRMs can also be separated. This active attraction and separation feature endows the RMCR with greater tip flexibility compared with a normal MCR, which may enable some unforeseen functionalities. The contributions can be summarized as follows:

1) propose a magnetic reprogramming method for MCR using shape memory alloy spring, propose a methodology to help the design of RMCR by analyzing the reprogramming process.
2) fabricate a RMCR under the guidance of the proposed methodology, and characterization of RMCR elements.
3) kinematic modeling and experimental validation of RMCR, workspace comparison between RMCR and normal MCR.

II. Design and Modeling

A. Overview of RMCR

Fig.1 illustrates the schematic diagram of the RMCR. It is composed of a flexible body and several MRMs. The flexible body is made of silicone rubber with an inner channel for heating wires and tools, as shown in Fig.1(c). Different segments of flexible body are connected through MRMs, which are the driving units of the RMCR. Fig.1(d) shows the structure of the MRM. An radially magnetized ring-shaped magnet is installed in the MRM. Like normal MCRs, when subjected to different external magnetic fields, the produced magnetic forces and torques will deform the RMCR to different shapes. However, unlike normal MCRs, the magnet inside the MRM is not completely fixed, it can rotate around a NiTi wire. In order to actively regulate the rotation of the magnet, two springs are connected to a magnet housing outside the magnet. The shape memory alloy spring (SMAS) is used for actuation and the steel wire spring (SWS) is used for preload. Shape memory alloys (SMA) are widely used in soft robot due to its high work density, compact structure, and low-actuated voltage [37]. When heated above a certain temperature, SMA will transform to its memory shape. The preload of SWS forces the magnet inside the MRM to return to the initial position when SMAS cools down. The entire MRM is encapsulated by a resin shell, which is also used to fix two ends of the NiTi wire.

The working principle of the MRM is shown Fig. 1(e). In the unactuated state, the SMAS relaxes and the magnet keep still under the preload of SWS. When heated beyond a certain temperature, the SMAS will contract and overcome the external force to rotate the magnet around the NiTi wire, thus changing the direction of the magnetic moment of the MRM. The RMCR has two working modes. In the first working mode, the external magnetic field remains unchanged. By actively reprogramming the magnetic moment of the MRM, the produced magnetic force $\mathbf{F}_m$ and moment $\mathbf{T}_m$ will deform the RMCR into different shapes. Multiple MRMs can be selectively or cooperatively reprogrammed to achieve a desired shape. In the second working mode, by changing the external magnetic field, the RMCR is controlled integrally. Combining the mentioned two modes, the RMCR can deform versatilely in different ways for complex scenarios.

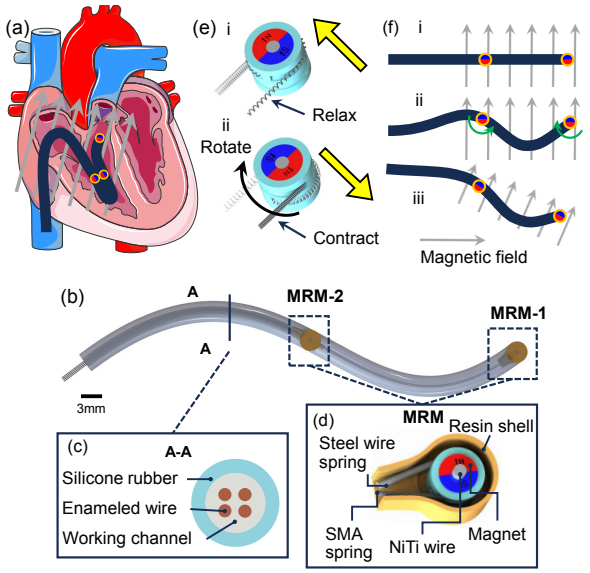

Fig. 1. Schematic diagram of reprogrammable magnetic continuum robot (RMCR). (a) Potential application scenery of the RMCR. (b) Structure overview of the proposed RMCR. The RMCR includes flexible body and several magnetic reprogramming modules (MRM). (c) Cross-section of the flexible body. The flexible body is made of silicone rubber sheath with a working channel. The inner channel is saved for heating wires and tools. (d) Close-up view of the MRM. The whole structure is encapsulated by resin shells. An axially magnetized ring-shaped magnet can rotate around a NiTi wire. Two springs are connected to the magnet shell, including a steel wire spring (SWS) for preloading and a shape memory alloy spring (SMAS) for actuation. (e) Magnetization reprogramming principle. i. In the unactuated state, the SMAS relaxes. ii. In the actuated state, the SMAS is heated and contracts, causing the magnet to rotate with the magnet housing, thus changing the direction of the magnetic moment. (f) Working process of RMCR. i. Initial state. ii. Actively programming the direction of magnetization of the MRM will deform the RMCR. iii. The shape of the RMCR can be further adjusted by changing the external magnetic field.

B. Force Analysis

Fig. 2 shows the force analysis of MRM. In the initial state, MRM has the following force equilibrium: $F_{s2} = F_{s1} + f_s$, where F_{s1} and F_{s2} are forces produced by SWS and SMAS, respectively, and f_s is the friction force between magnet and central NiTi wire. When heating SMA, F_{s1} will increase and cause the magnet to rotate around the NiTi wire. Thus, we have $F_{s2} > F_{s1} + f_s$, where f_s changes from static friction to sliding friction. Applying an external magnetic

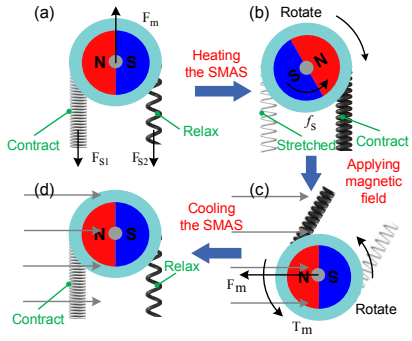

Fig. 2. Force analysis of MRM. (a) Initial state. The MRM is in equilibrium under the spring force F_{s1}, F_{s2} and the friction force f_s. (b) SMAS contracts when heated. Once F_{s2} is large enough, the magnet will rotate around the central NiTi wire. (c) Applying magnetic force, the MRM will rotate under the magnetic force F_m and torque T_m. (d) SMAS will relax when cools down. The magnet will gradually recover under spring preload, causing the MRM to rotate to its initial position under magnetic torque.

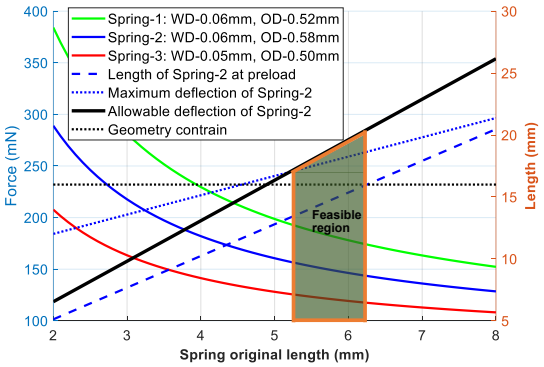

Fig. 3. Design principle of the MRM. The shaded area represents the region consisting of the feasible spring parameters. It considers the maximum deflection of the spring and the geometrical limits of the MRM. The rightmost shaded area represents the optimal spring length, since the spring has smaller stiffness and allows the magnet to rotate with less driving force.

field, the magnetic force $\mathbf{F}_m$ and torque $\mathbf{T}_m$ will cause the rotation of the MRM. $\mathbf{F}_m$ and $\mathbf{T}_m$ can be calculated as:

$$\mathbf{F}_m = \nabla(\mathbf{b}\cdot\mathbf{m}), \quad \mathbf{T}_m = \mathbf{m}\times\mathbf{b}, \tag{1}$$

where $\mathbf{b}$ is the magnetic field and $\mathbf{m}$ is the magnetic moment.

When cooling down, SMAS will gradually relax and the magnet will rotate because the reduced F_{s2} is insufficient to keep the magnet stationary, therefore, we have $F_{s1} > F_{s2} + f_s$. When attached to the flexible body of RMCR, the MRM will not rotate freely, its rotation will cause the deformation of the RMCR.

C. Design Methodology

As we mentioned before, the main function of the SWS is to provide a preload to initialize the position of MRM. Smaller stiffness of SWS may provide insufficient preload force while larger stiffness may generate large spring force and hinder the rotation of the magnet. Therefore, the choice of the SWS is very important. Here, we propose a strategy for choosing SWS parameters and designing MRM.

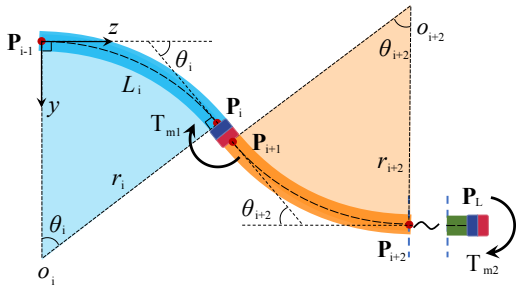

Fig. 4. Schematic diagram of piecewise constant curvature model. The magnet segments ($\mathbf{P}_i - \mathbf{P}_{i+1}$ and $\mathbf{P}_{L-1} - \mathbf{P}_L$) are represented by a rigid rod.

First, we introduce some formulas related to springs. The stiffness of a tension spring can be calculated as follows:

$$K = \frac{Gd^4 g}{8000 D_m^3 N}, \tag{2}$$

where G, d, D_m and N are parameters related to the SWS spring, G is the shear modulus, d is the wire diameter, D_0 is the outer diameter, N is the spring turns and $D_m = D_0 - d$ is the middle diameter. g is the gravity acceleration and the unit of K in (2) is mN/mm. The shear stress in an extension spring can be calculated as:

$$\tau = \frac{8K_w F D_m}{\pi d^3}, \tag{3}$$

where, $F = K\Delta x$ is the force applied on the spring. K_w is the Wahl Correction Factor [38]:

$$K_w = \frac{4C-1}{4C-4} + \frac{0.615}{C}, \tag{4}$$

where $C = D/d$ is the spring index. Combining (2)(3) and (4), the maximum extension length of a spring γ is:

$$\gamma = \pi N d \frac{\tau_{\max} D_m^2}{K_w G d^2} \tag{5}$$

where $\tau_{\max}$ is the maximum shear stress of the material.

Equations (2) and (5) established the property of a tension spring, combining with the parameters of SMAS, we can get the feasible design area as shown in Fig.3. The shadow area means that SWS satisfies the following conditions:

a: The length of the SWS at preload does not exceed the geometry of the MRM.

b: The maximum displacement of SWS when EPM rotates to the maximum angle does not exceed the maximum allowable elongation of SWS.

D. Kinematic Modeling of RMCR

Kinematic modeling of a magnetic continuum robot is important and challenging. We assume that the actuation magnetic field is homogeneous, which is the same as during the experiment, according to (1), the MRMs will be only subject to magnetic torque. We propose to use 2D piecewise constant curvature (PCC) model [39] and force-equlibrium based approach to model and solve the kinematics of an RMCR, as shown in Fig.4. The bending curvature $\kappa_i = 1/r_i$ of the flexible body can be calculated as: $\kappa_i = T_i/E_i I_i$, where T_i is the torque, E_i is the Young's modulus, and

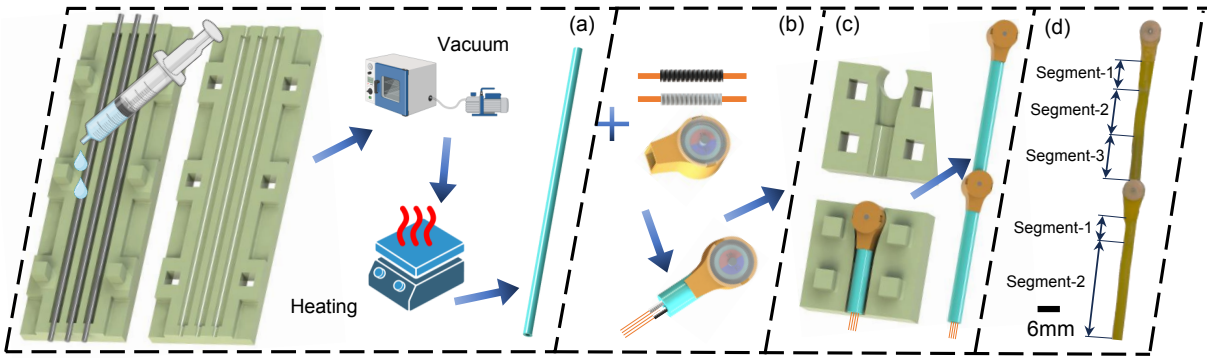

Fig. 5. Fabrication process of the RMCR. (a) Fabrication of silicone tube. First, NiTi rods are placed on the lower mold. Then, the mixed silicone rubber is poured on top of the mold, and then vacuumed and heated for curing. After curing, the silicone tube is obtained by removing the middle NiTi rod. (b) Fabrication of MRM. The assembled springs are connected to the magnet housing. MRMs are then attached to a shorter silicone tube. (c) Sealing process. The assembled MRM is then mold-assisted to cure a layer of silicone for sealing. (d) Prototype of RMCR. RMCR has two MRMs and the diameter of MRM is 6mm. The overall length of RMCR is 95mm. The parameters of RMCR are listed in Table.I

I_i is the second area moment of the i^{th} segment. According to the geometrical relationship, the ending position $\mathbf{P}_i^l = [0\ p_{y,i}\ p_{z,i}]^T$ of a segment in the local frame can be calculated as:

$$p_{y,i}^l = -\kappa_i^{-1}(1 - cos(\theta_i)), \quad p_{z,i}^l = ||\kappa_i^{-1}||sin(\theta_i), \tag{6}$$

where $\theta_i = L_i/r_i$, and L_i is the arc length of the i^{th} segment. Then $\mathbf{P}_i^l$ can be translated into the global frame by the homogeneous transformation matrix ${}_w^l\mathbf{T}_i$:

$${}_w^l\mathbf{T}_i = \begin{bmatrix} {}_w^l\mathbf{R}_i & {}_w^l\mathbf{P}_i \\ \mathbf{0}_1 & 1 \end{bmatrix} \tag{7}$$

where ${}_w^l\mathbf{P}_i = [0\ p_{y,i-1}\ p_{z,i-1}]$ is the ending point of the $i^{th}-1$ segment and ${}_w^l\mathbf{R}_i \in SO(3)$ is the rotation matrix. The MRM can be regarded as a rigid rod and the curvature of its right and left boundaries has the following relationship:

$$\kappa_i^+ = \kappa_i^- + T_{m,x}E_i^{-1}I_i^{-1}. \tag{8}$$

where $T_{m,x}$ is the x-axis component of $\mathbf{T}_m$. By guessing the bending curvature of the first segment κ_i, the kinematic model can be solved by using shooting method combined with an optimization function:

$$\min_{\kappa_1} \quad \kappa_L - T_{m2}E_L^{-1}I_L^{-1}, \tag{9}$$

where κ_L is the bending curvature of the last arc and T_{m2} is the magnetic torque applied to the tip magnet. Equation (9) can be solved by using $fmincon$ function in MATLAB.

III. Fabrication Process

1) Fabrication of the Springs: The SWS are connected to enameled wires (wire diameter 0.08 mm) and bonded with light-curing adhesive (Ergo-8500). Two peeled enameled wires are connected to the two ends of the SMAS, and then placed on a fixture to apply pre-stress to straighten it. Then the connection point is evenly applied with silicone rubber.

TABLE I
Parameters of the RMCR

Parts	MRM	Segment-1	Segment-2	Segment-3
Diameter/ Width	6mm	D = 3mm, d = 1.5mm	D = 3mm, d = 1.5mm	D = 3mm, d = 1.5mm
Length	15mm	10mm	13, 26mm	12mm
Materials	Resin	Dragon Skin30	Ecoflex 30	Dragon Skin30

D = outer diameter, d = inner diameter.

2) Fabrication of the MRM: First, the 3D-printed magnet housing is connected to the two springs through positioning holes. Then, an axially-magnetized ring-shaped permanent magnet (D = 3 mm, d = 1 mm, h = 3.3 mm) is then bonded to the magnet housing. After fixing to the outer shell, the central NiTi wire is passed through the inner hold of the magnet. Finally, covering the MRM with another half of shell, the magnet can rotate freely around the central wire. The outer shell and the magnet housing was made of photosensitive resin using a high-resolution 3D printer (Saturn 3 Ultra).

3) Fabrication of the Flexible Segments: The flexible segments are fabricated through casting process. First, 1.5 mm diameter NiTi rods are placed on the lower mold through positioning holes. Then, the mixed silicone rubber is then poured to the mold and put into an oven under 40°C for 30min and 80°C for 30 min. Finally, a hollow flexible segment can be obtained by demolding the cured silicone. The stiffness of the flexible body can be adjusted by using different silicone rubber. The parameters of the RMCR are listed in Table I

4) Assembly Process: The MRM was placed on a mold to cure a layer of silicone for sealing, as shown in Fig.5(c). Different parts are connected by silicon rubber and adhesive.

IV. Experimental Results and Discussion

A. Characterization of the SMAS

The SMAS will contract once heated beyond a certain temperature and soften when cools down. In the soften state, SMAS produces plastic rather than elastic deformation under external force. We empirically tested the stiffness of

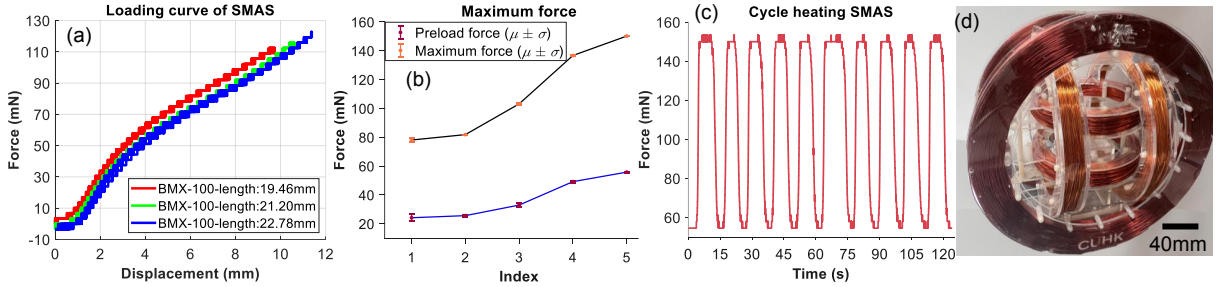

Fig. 6. Characterization of SMAS. (a) Loading curve of SMAS. (b) Maximum force produced by SMAS at different preload. (Error bar denotes the SD from three experiments). (c) Cycle heating curve of SMAS. (d) Helmholtz coil system (HCS) used in experiments.

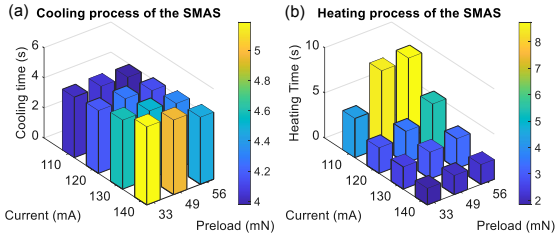

Fig. 7. Heating and cooling characteristics of SMAS at different current and preload. (a) Heating property. (b) Cooling property.

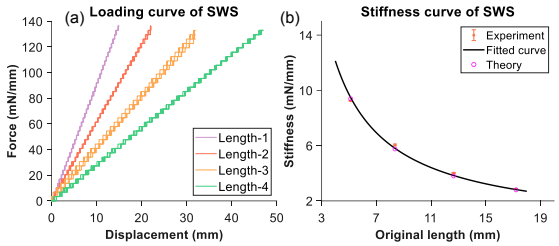

Fig. 8. Property of the steel wire spring (SWS). (a) The loading curves for the five experiments. Different force biases are used to distinguish different experiments. (b) Experimentally obtained spring stiffness, and stiffness curves fitted using an inverse proportional function. (Error bar denotes the SD from three experiments)

SMAS using a mechanical tester (MACH-1 mechanical tester v500cst, MA008). One end of the SMAS was fixed to a 10 N load cell and the other is fixed to a moving stage. First, we test the loading curve of the SMAS at different lengths as shown in Fig.6(a). The loading curves are not straight lines, which means the stiffness of the SMASs is constantly changing. A longer spring, however, requires less force to produce the same displacement.

Fig.6(b) shows the maximum force produced by SMAS at different preloads. A tension spring is connected in series with the SMAS to allow full contraction of the SMAS. The stage was set to apply different preload to the SMAS. Then, a 150 mA current was fed to energize the SMAS to produce the maximum force. Results show that larger preload produce larger maximum contract force. This is because higher preload allows SMAS to produce more plastic deformation, which allows for greater displacement during contraction. Fig.6(c) shows that the force generated by SMAS remains unchanged after 10 cycles of heating and cooling.

Fig.7 shows the response time of SMAS at different situation. The heating speed is mainly related to the magnitude of the current. Higher preload slightly increase the heating time, this may be related to the larger contraction travel. At a current of 110 mA, the states with preload of 49 mN and 56 mN may be in a critical heating state, resulting in a longer heating time. The cooling time slightly increases with a larger current and smaller preload. The sum of the cooling and heating times is about 10 s, which means that the RMCR can be reprogrammed in just over 10 s. The maximum temperature of the SMAS is about 80°C and can be reduced by coating materials with low thermal conductivity.

B. Characterization of the SWS

Fig.8(a) shows the loading curve of the SWS. Equation (2) indicates that the stiffness of a spring is inversely proportional to its length. Therefore, we use function $y = a/x$ to fit the spring stiffness. This is achieved by using the curve fitting tool in MATLAB. The fitting result is $a = 48.54$ with an R^2 of 0.9937 and a RMSE of 0.22. Fig.8(b) shows the experimental results and the fitted curve.

C. 2D Experiments

To demonstrate the functionalities of the proposed RMCR, we performed the 2D experiments in a Helmholtz coil system (HCS) as shown in Fig.6(d). The HCS is composed of three orthogonal arranged coils. It has a workspace about $80\times80\times80$ mm^3 and a magnetic field strength of 0-8 mT. Fig.9 shows the moving sequence of RMCR as:

1) Step-1: We first applied a 4 mT magnetic field. By in-situ reprogramming the magnetic moment of the MRM-1 from 90° to -135°, RMCR gradually changed to a C shape under magnetic torque, as shown in Fig.9(a) and (h).

2) Step-2: The magnetic moment of the MRM-2 was then reprogrammed to rotate from 90° to 135°. The RMCR was further deformed and the distance between MRM-1 and MRM-2 gradually decreased. When smaller than a threshold, the magnetic attraction between these two modules overcame the elastic force of flexible body and the two modules will stick together, as shown in Fig.9(b) and (i).

3) Step-3: After sticking together, MRM-1 and MRM-2 worked as a single unit. By rotating the direction of the magnetic field, RMCR also rotated while keeping MRM-1 and 2 unseparated, like mode-2 illustrated in Fig.1(f).

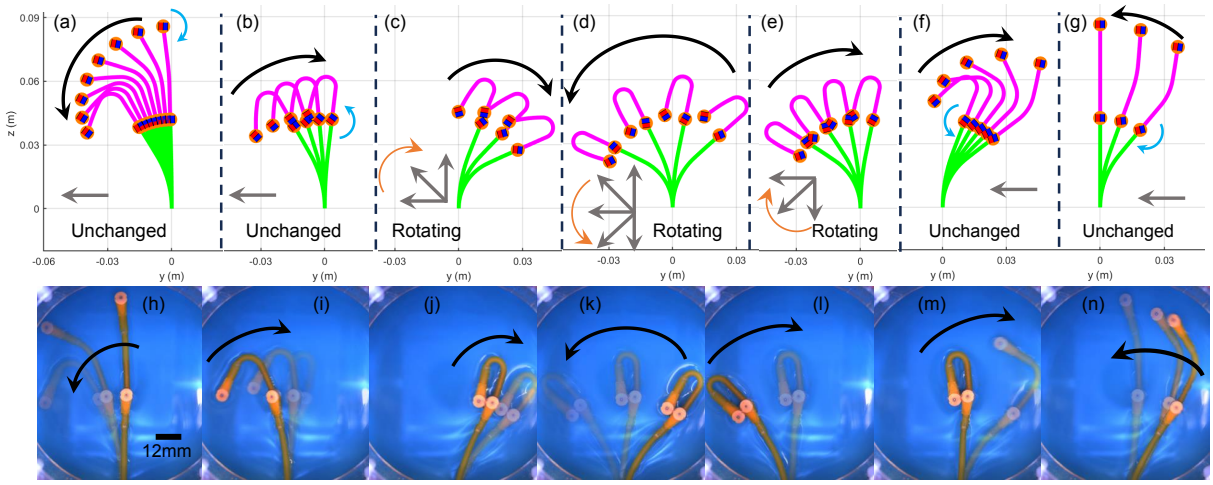

Fig. 9. Simulation and experiments results. (a)-(g). Simulated moving sequence. (h)-(n). Corresponding moving sequence of RMCR in experiments.

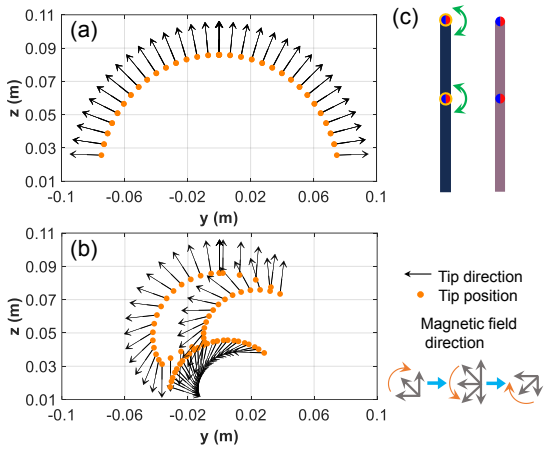

Fig. 10. Workspace comparison between RMCR (a) and MCR (b). (c) The RMCR and MCR has the same parameters, the only difference is whether or not the magnet can be reprogrammed.

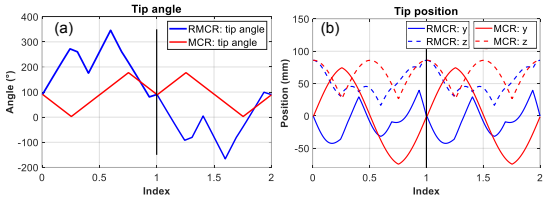

Fig. 11. Comparison of tip angle (a) and tip position (b) between RMCR and normal MCR. By rotating the base of the robot, its workspace can be expanded. The left and right sides of the solid black line represent the workspace before and after the base is rotated 180°, respectively.

Fig.9(c)-(e) and (j)-(l) show the rotating process of the RMCR. The external magnetic field was first rotated 90° clockwise, then 180° counterclockwise, and finally 90° clockwise to the initial position. MRM-1 and 2 remain unseparated during the entire process.

4) Step-4: Fig.9(f) and (m) show that, the magnetic field remain unchanged and by counterclockwise reprogramming MRM-1, the attractive force between MRM-1 and MRM-2 started to decrease. When the force cannot resist the elastic force of the flexible body, MRM-1 and MRM-2 separated.

5) Step-5: As shown in Fig.9(g) and (n), by clockwise reprogramming MRM-2, RMCR gradually became straight under magnetic field, just like the inverse process of Step-1.

D. Comparison of the Workspace

Fig.10 compared the workspace of RMCR and MCR through simulation. Parameters of the robots are listed in Table I. The strength of the actuation magnetic field is 4mT and the moving sequence is the same as in Fig.9. The tip trajectory of MCR is nearly semicircular, and the tip direction is almost the same as the external magnetic field. However, the tip of the RMCR is more flexible, it consists of four parts of arcs of different radii. The corresponding tip angles and positions are shown in Fig.11. The normal MCR has a tip angle range of 0° to 173°, while the RMCR has a range of -166° to 343°, which increases by 193%. Compared with MCR, RMCR has a more centralized tip position but a greater range of tip directions, which means RMCR can achieve more complex deformations in tighter spaces.

V. Conclusion

In this paper, we introduced a RMCR capable of real-time in-situ magnetic reprogramming. The robot can achieve large deformations under external magnetic field, including the active attraction and separation motion which enhance the tip dexterity. A kinematic model was established to estimate the equilibrium shape of RMCR. We theoretically modeled the elements in the MRM and proposed a methodology to guide the design process of the RMCR. A RMCR prototype was fabricated accordingly and tested with experiments. Results show that the proposed modeling approach has a good agreement with the experiments. Compared with a regular MCR, the tip position of RMCR is more centralized and the tip range of change in direction increased by 193%, which means that the RMCR can achieve greater tip direction change in a smaller area. However, more work is needed to optimize the structure of RMCR and to achieve precise reprogramming control.

REFERENCES

[1] B. J. Nelson, S. Gervasoni, P. W. Chiu, L. Zhang, and A. Zemmar, "Magnetically actuated medical robots: An in vivo perspective," *Proceedings of the IEEE*, vol. 110, no. 7, pp. 1028–1037, 2022.

[2] M. Runciman, A. Darzi, and G. P. Mylonas, "Soft robotics in minimally invasive surgery," *Soft robotics*, vol. 6, no. 4, pp. 423–443, 2019.

[3] Y. Kim, G. A. Parada, S. Liu, and X. Zhao, "Ferromagnetic soft continuum robots," *Science Robotics*, vol. 4, no. 33, p. eaax7329, 2019.

[4] Z. Yang, L. Yang, M. Zhang, C. Zhang, S. C. H. Yu, and L. Zhang, "Ultrasound-guided catheterization using a driller-tipped guidewire with combined magnetic navigation and drilling motion," *IEEE/ASME transactions on mechatronics*, vol. 27, no. 5, pp. 2829–2840, 2021.

[5] J. Lussi, M. Mattmann, S. Sevim, F. Grigis, C. De Marco, C. Chautems, S. Pané, J. Puigmartí-Luis, Q. Boehler, and B. J. Nelson, "A submillimeter continuous variable stiffness catheter for compliance control," *Advanced Science*, vol. 8, no. 18, p. 2101290, 2021.

[6] S. L. Charreyron, Q. Boehler, B. Kim, C. Weibel, C. Chautems, and B. J. Nelson, "Modeling electromagnetic navigation systems," *IEEE Transactions on Robotics*, vol. 37, no. 4, pp. 1009–1021, 2021.

[7] L. Yang, J. Jiang, X. Gao, Q. Wang, Q. Dou, and L. Zhang, "Autonomous environment-adaptive microrobot swarm navigation enabled by deep learning-based real-time distribution planning," *Nature Machine Intelligence*, vol. 4, no. 5, pp. 480–493, 2022.

[8] J. Sikorski, A. Denasi, G. Bucchi, S. Scheggi, and S. Misra, "Vision-based 3-d control of magnetically actuated catheter using bigmag—an array of mobile electromagnetic coils," *IEEE/ASME transactions on mechatronics*, vol. 24, no. 2, pp. 505–516, 2019.

[9] K. B. Yesin, K. Vollmers, and B. J. Nelson, "Modeling and control of untethered biomicrorobots in a fluidic environment using electromagnetic fields," *The International Journal of Robotics Research*, vol. 25, no. 5-6, pp. 527–536, 2006.

[10] W. Hu, G. Z. Lum, M. Mastrangeli, and M. Sitti, "Small-scale soft-bodied robot with multimodal locomotion," *Nature*, vol. 554, no. 7690, pp. 81–85, 2018.

[11] M. Zhang, L. Yang, C. Zhang, Z. Yang, and L. Zhang, "A 5-d large-workspace magnetic localization and actuation system based on an eye-in-hand magnetic sensor array and mobile coils," *IEEE Transactions on Instrumentation and Measurement*, vol. 72, pp. 1–11, 2023.

[12] J. Sikorski, C. M. Heunis, R. Obeid, V. K. Venkiteswaran, and S. Misra, "A flexible catheter system for ultrasound-guided magnetic projectile delivery," *IEEE transactions on robotics*, vol. 38, no. 3, pp. 1959–1972, 2021.

[13] Z. Yang, L. Yang, M. Zhang, N. Xia, and L. Zhang, "Ultrasound-guided wired magnetic microrobot with active steering and ejectable tip," *IEEE Transactions on Industrial Electronics*, vol. 70, no. 1, pp. 614–623, 2022.

[14] G. Pittiglio, M. Brockdorff, T. da Veiga, J. Davy, J. H. Chandler, and P. Valdastri, "Collaborative magnetic manipulation via two robotically actuated permanent magnets," *IEEE Transactions on Robotics*, vol. 39, no. 2, pp. 1407–1418, 2022.

[15] Y. Kim, E. Genevriere, P. Harker, J. Choe, M. Balicki, R. W. Regenhardt, J. E. Vranic, A. A. Dmytriw, A. B. Patel, and X. Zhao, "Telerobotic neurovascular interventions with magnetic manipulation," *Science Robotics*, vol. 7, no. 65, p. eabg9907, 2022.

[16] G. Pittiglio, J. H. Chandler, T. da Veiga, Z. Koszowska, M. Brockdorff, P. Lloyd, K. L. Barry, R. A. Harris, J. McLaughlan, C. Pompili, and P. Valdastri, "Personalized magnetic tentacles for targeted photothermal cancer therapy in peripheral lungs," *Communications Engineering*, vol. 2, no. 1, p. 50, 2023.

[17] Q. Wang, K. F. Chan, K. Schweizer, X. Du, D. Jin, S. C. H. Yu, B. J. Nelson, and L. Zhang, "Ultrasound doppler-guided real-time navigation of a magnetic microswarm for active endovascular delivery," *Science Advances*, vol. 7, no. 9, p. eabe5914, 2021.

[18] T. Wang, H. Ugurlu, Y. Yan, M. Li, M. Li, A.-M. Wild, E. Yildiz, M. Schneider, D. Sheehan, W. Hu, and M. Sitti, "Adaptive wireless millirobotic locomotion into distal vasculature," *Nature communications*, vol. 13, no. 1, p. 4465, 2022.

[19] S. Salmanipour, O. Youssefi, and E. D. Diller, "Design of multi-degrees-of-freedom microrobots driven by homogeneous quasi-static magnetic fields," *IEEE Transactions on Robotics*, vol. 37, no. 1, pp. 246–256, 2020.

[20] L. B. Kratchman, T. L. Bruns, J. J. Abbott, and R. J. Webster, "Guiding elastic rods with a robot-manipulated magnet for medical applications," *IEEE Transactions on Robotics*, vol. 33, no. 1, pp. 227–233, 2016.

[21] J. Wang, J. Xue, S. Yuan, J. Tan, S. Song, and M. Q.-H. Meng, "Kinematic modeling of magnetically-actuated robotic catheter in nonlinearly-coupled multi-field," *IEEE Robotics and Automation Letters*, vol. 6, no. 4, pp. 8189–8196, 2021.

[22] J. Edelmann, A. J. Petruska, and B. J. Nelson, "Magnetic control of continuum devices," *The International Journal of Robotics Research*, vol. 36, no. 1, pp. 68–85, 2017.

[23] S. Jeon, A. K. Hoshiar, K. Kim, S. Lee, E. Kim, S. Lee, J.-y. Kim, B. J. Nelson, H.-J. Cha, B.-J. Yi, and H. Choi, "A magnetically controlled soft microrobot steering a guidewire in a three-dimensional phantom vascular network," *Soft robotics*, vol. 6, no. 1, pp. 54–68, 2019.

[24] M. Richter, V. K. Venkiteswaran, and S. Misra, "Multi-point orientation control of discretely-magnetized continuum manipulators," *IEEE Robotics and automation letters*, vol. 6, no. 2, pp. 3607–3614, 2021.

[25] D. Lin, W. Chen, K. He, N. Jiao, Z. Wang, and L. Liu, "Position and orientation control of multisection magnetic soft microcatheters," *IEEE/ASME Transactions on Mechatronics*, vol. 28, no. 2, pp. 907–918, 2022.

[26] D. Lin, N. Jiao, Z. Wang, and L. Liu, "A magnetic continuum robot with multi-mode control using opposite-magnetized magnets," *IEEE Robotics and Automation Letters*, vol. 6, no. 2, pp. 2485–2492, 2021.

[27] J. Hwang, S. Jeon, B. Kim, J.-y. Kim, C. Jin, A. Yeon, B.-J. Yi, C.-H. Yoon, H.-J. Park, S. Pané, B. J. Nelson, and H. Choi, "An electromagnetically controllable microrobotic interventional system for targeted, real-time cardiovascular intervention," *Advanced Healthcare Materials*, vol. 11, no. 11, p. 2102529, 2022.

[28] G. Pittiglio, P. Lloyd, T. da Veiga, O. Onaizah, C. Pompili, J. H. Chandler, and P. Valdastri, "Patient-specific magnetic catheters for atraumatic autonomous endoscopy," *Soft Robotics*, vol. 9, no. 6, pp. 1120–1133, 2022.

[29] Z. Yang, L. Yang, M. Zhang, Q. Wang, S. C. H. Yu, and L. Zhang, "Magnetic control of a steerable guidewire under ultrasound guidance using mobile electromagnets," *IEEE Robotics and Automation Letters*, vol. 6, no. 2, pp. 1280–1287, 2021.

[30] J. Tan, J. Xue, X. Yang, S. Yuan, W. Liu, H. Ren, S. Song, and J. Wang, "Model-free and uncalibrated visual-feedback control of magnetically-actuated flexible endoscopes," in *2022 IEEE/RSJ International Conference on Intelligent Robots and Systems (IROS)*. IEEE, 2022, pp. 5930–5936.

[31] Y. Dong, L. Wang, Z. Zhang, F. Ji, T. K. Chan, H. Yang, C. P. Chan, Z. Yang, Z. Chen, W. T. Chang, J. Y. Chan, J. J. Sung, and L. Zhang, "Endoscope-assisted magnetic helical micromachine delivery for biofilm eradication in tympanostomy tube," *Science Advances*, vol. 8, no. 40, p. eabq8573, 2022.

[32] Y. Kim, H. Yuk, R. Zhao, S. A. Chester, and X. Zhao, "Printing ferromagnetic domains for untethered fast-transforming soft materials," *Nature*, vol. 558, no. 7709, pp. 274–279, 2018.

[33] N. Xia, D. Jin, C. Pan, J. Zhang, Z. Yang, L. Su, J. Zhao, L. Wang, and L. Zhang, "Dynamic morphological transformations in soft architected materials via buckling instability encoded heterogeneous magnetization," *Nature Communications*, vol. 13, no. 1, p. 7514, 2022.

[34] Y. Alapan, A. C. Karacakol, S. N. Guzelhan, I. Isik, and M. Sitti, "Reprogrammable shape morphing of magnetic soft machines," *Science advances*, vol. 6, no. 38, p. eabc6414, 2020.

[35] Y. Cao, Z. Yang, B. Hao, X. Wang, M. Cai, Z. Qi, B. Sun, Q. Wang, and L. Zhang, "Magnetic continuum robot with intraoperative magnetic moment programming," *Soft Robotics*, 2023, 10.1089/soro.2022.0202.

[36] J. Cui, T.-Y. Huang, Z. Luo, P. Testa, H. Gu, X.-Z. Chen, B. J. Nelson, and L. J. Heyderman, "Nanomagnetic encoding of shape-morphing micromachines," *Nature*, vol. 575, no. 7781, pp. 164–168, 2019.

[37] X. Huang, M. Ford, Z. J. Patterson, M. Zarepoor, C. Pan, and C. Majidi, "Shape memory materials for electrically-powered soft machines," *Journal of Materials Chemistry B*, vol. 8, no. 21, pp. 4539–4551, 2020.

[38] P. Tan, A. Akhavan Farid, A. Karimzadeh, S. S. Rahimian Koloor, and M. Petr, "Investigation on the curvature correction factor of extension spring," *Materials*, vol. 13, no. 18, p. 4199, 2020.

[39] R. J. Webster III and B. A. Jones, "Design and kinematic modeling of constant curvature continuum robots: A review," *The International Journal of Robotics Research*, vol. 29, no. 13, pp. 1661–1683, 2010.